PERGAMON

Aerosol Science 34 (2003) 1421–1444

Journal of
Aerosol Science

www.elsevier.com/locate/jaerosci

UV-VIS-NIR spectral optical properties of soot and soot-containing aerosols

M. Schnaiter[a,*], H. Horvath[b], O. Möhler[a], K.-H. Naumann[a], H. Saathoff[a], O.W. Schöck[a]

[a] *Forschungszentrum Karlsruhe, Institut für Meteorologie und Klimaforschung, Postfach 3640, D-76021 Karlsruhe, Germany*
[b] *Institut für Experimentalphysik der Universität Wien, Boltzmanngasse 5, A-1090 Vienna, Austria*

Received 20 January 2003; accepted 14 June 2003

Abstract

The UV-VIS-NIR spectral optical properties of soot and soot containing aerosols were investigated in detail during the AIDA Soot Aerosol Campaign 1999. One aim of the campaign was a comprehensive comparison of the microphysical properties of Diesel and spark generator soot. The mass specific extinction cross section at $\lambda=$ 450 nm of Diesel soot is 10.6 ± 0.5 m^2 g^{-1} which is almost a factor of two larger than the corresponding value of 5.7 ± 0.3 m^2 g^{-1} measured for spark generator soot. Coagulation-induced particle growth does not affect the soot extinction cross section and has a weak influence on the scattering properties of the soot aggregates. Atmospheric processing of freshly emitted soot was simulated in mixing experiments. The formation of mixed Diesel soot and dry ammonium sulfate particles by coagulation has only a minor effect on the soot absorption cross section. The coating of spark generated soot with organic material results in a strong increase of the single scattering albedo. A significant increase of the absorption coefficient at $\lambda=473$ nm during the coating process can be attributed to an enhancement of the specific soot absorption cross section by more than 30%.

1. Introduction

The atmospheric absorption of solar radiation by aerosols in the visible is mainly due to soot and to mineral dust. Thus, the absorption properties of airborne soot and soot containing aerosols may influence directly the atmospheric visibility as well as local and global climate. The direct positive shortwave forcing by soot is of particular concern since it may decrease significantly the total negative

* Corresponding author.
E-mail address: martin.schnaiter@imk.fzk.de (M. Schnaiter).

0021-8502/$ - see front matter © 2003 Elsevier Ltd. All rights reserved.
doi:10.1016/S0021-8502(03)00361-6

forcing attributed to sulfate aerosols especially in future emission scenarios in which the sulfate aerosol concentrations decrease due to regulations aimed at reducing acid rain (Hansen, Sato, Ruedy, Lacis, & Oinas, 2000). Several investigations were performed on the shortwave climatic impact of the atmospheric aerosol, showing that it is comparable in magnitude but negative in sign to the longwave forcing by anthropogenic greenhouse gases (Charlson et al., 1992; IPCC 2001). Radiative transfer models used in these investigations to predict the direct forcing by aerosols are based on spectral optical properties calculated by Mie-Theory. While this is a reasonable approach for spherical particles like aqueous sulfate aerosol, soot particles possess a rather complex fractal-like morphology which makes a reliable modeling of their optical properties much more difficult. Moreover, the mixing state of soot in the atmospheric aerosol is usually assumed to be external, which overestimates the above net cooling effect significantly. This was shown recently by Jacobson (2001) using a global circulation model which accounts for atmospheric processing of the aerosol. To judge by that, the net heating effect of atmospheric soot may be comparable or even exceed that due to methane, the second most important greenhouse gas.

1.1. Optics of fractal soot aggregates

The extinction properties of soot aggregates composed of $N=3$–1390 primary spheres or monomers were approximated recently by coupled dipole calculations (Mulholland & Mountain, 1999). The variation of the mass specific absorption and extinction cross sections σ_a, σ_e with aggregate size was found to be dependent mainly on the size parameter $x_p = \pi d_p/\lambda$, which is the ratio between the monomer circumference and the wavelength of light. This value was varied in the range from 0.05 to 0.6. For the smallest size parameter investigated, $x_p = 0.05$, the single scattering albedo ω_0, which is the ratio of the mass specific scattering to extinction cross section σ_s/σ_e, was found to be less than 0.02 even for the largest aggregates. For size parameters typical for atmospheric soot primaries and visible wavelengths ($x_p = 0.2$–0.3), larger ω_0 values between 0.1 and 0.2 were calculated for aggregates composed of $N=100$ to 1000 primaries. Here, it should be noted that the same refractive index $m = 1.7 + i0.7$ was assumed for all calculations. For large aggregates and for primary size parameters $x_p \geqslant 0.2$ the specific absorption cross section decreases significantly as a result of screening within the aggregate. For small clusters a calculated aggregation absorption enhancement of about 10% with respect to the isolated monomers is primarily the result of the electromagnetic coupling between the monomers. The analysis of the size dependence of the specific absorption cross section has shown that the coupling is very strong between the nearest neighbors and decreases very rapidly for primaries having larger distances within the aggregate. This is in good agreement with experimental results by Schnaiter, Mutschke, Dorschner, Henning, and Salama (1998) for matrix isolated soot primaries and small aggregates. Thus, the extinction properties of large soot aggregates as they are typical for flames and Diesel engine exhaust may be approximated quite well by theories neglecting the electromagnetic coupling within the aggregates like the Rayleigh–Debye–Gans (RDG) approximation (e.g. Dobbins & Megaridis, 1991). This approximation is widely used to determine the aggregate structure from scattering measurements (e.g. Sorensen, Cai, & Lu, 1992). One of the main results of the RDG approximation namely the near constancy of σ_e with the number of primaries per aggregate for aggregates composed of more than $\sim$100 monomers was confirmed experimentally by Dobbins, Mulholland, and Bryner (1994) for airborne flame soot grown by coagulation in an aerosol chamber.

1.2. Electronic structure of soot material

The complex refractive index $m = n + ik$ of soot is not only a function of wavelength but also depends on the physical conditions and the chemical environment during its formation. An inter-comparison of experimentally determined refractive indices for different kinds of soot found in the literature is given by Fuller, Malm, and Kreidenweis (1999). According to this comparison refractive indices in the range from $1.50 + i0.50$ to $2.67 + i1.3$ at $\lambda = 550$ nm are typical for the different solid state structures of soot material.

The present knowledge about the linkage between the optical properties of carbonaceous solids and their solid state structure comes from different fields of research such as solid state physics, coal research, and laboratory astrophysics (Robertson & O'Reilly, 1987; Jäger, Henning, Schlögl, & Spillecke, 1999; Michel, Henning, Jäger, & Kreibig, 1999; Papoular et al., 1996; Mennella et al., 1995; Henning & Schnaiter, 1998). Soot material is characterized by a great structural variability. In contrast to the energetically more favorable crystalline structures of solid carbon, i.e. graphite or diamond, soot particles generally exhibit a structural order only on a mesoscopic scale ($\sim$1 nm). The term "disordered" is more preferable for the solid state structure of soot than the frequently used term "amorphous".

Most of the models for the internal structure of black carbon assume that nanocrystalline graphitic regions, the so-called basic structural units (BSUs), are embedded into the short-range order of the carbon network. Such structures have frequently been reported in high resolution transmission electron microscopy (HRTEM) investigations of soot samples (Jäger et al., 1999) and are also detectable in Diesel soot monomers (Wentzel et al., 2003). The finite size of the BSUs is responsible for the occurrence of a band gap in the density of electronic states of the material. This band gap decreases with BSU size and is expected to be typically between 0.2 and 5 eV for disordered solid carbon materials. Within a simple Hückel framework the UV-VIS-NIR absorption behavior of soot is explained by interband transitions between the filled valence (π) band and the empty conduction (π^*) band (Robertson & O'Reilly, 1987). Annealing experiments of deposited spark generated soot produced in a pure hydrogen atmosphere have shown that the absorption spectrum is sensitive to the annealing temperature, in a way that the position of the π–π^* transition maximum was shifted from 195 nm for the as produced samples to 260 nm for the samples annealed at 800°C (Mennella et al., 1995). They discussed the observed spectral changes as a structural change due to the hydrogen loss leading to an increase of delocalized π-electronic states in growing BSUs and, consequently, a decrease of the electronic band gap. Jäger et al. (1999) discussed the spectral optical properties of deposited soot, produced by quenching resistively heated graphite, in conjunction with its internal structure unraveled by HRTEM analysis. They reported a band position of $\sim$220 nm for samples with no detectable BSU structure and a position of $\sim$265 nm for structures composed almost entirely of plane randomly orientated BSUs. Altogether there is evidence for a linkage between the variability in medium-range BSU structure observed in disordered soot samples and the variability in their absorption properties, i.e. their refractive indices.

1.3. Specific absorption cross section of soot

A wide range of specific absorption cross sections σ_a between 3 and 25 $m^2\ g^{-1}$ is found in the literature (Liousse, Cachier, & Jennings, 1993). To assess and compare these values it is important to

note that the wavelength dependence of σ_a for soot is rather strong, leading to values at the blue limit of the visual spectrum which can be more than twice the value at the red limit (Moosmüller, Arnott, Rogers, Chow, & Frazier, 1998). Thus, the spread of absorption cross sections reported in the literature may be partly due to the range of wavelengths used in the measurements. However, a significant part of this spread is certainly due to the use of different methods and definitions for the determination of the soot mass concentration, as well as the uncertainties in filter based optical methods for the measurement of the soot absorption or attenuation especially in mixed aerosol samples (Saathoff et al., 2003a–c; Weingartner et al., 2003; Petzold, Kopp, & Niessner, 1997; Horvath, 1997). For pure spark discharge soot (Palas, model GFG 1000), which is widely used as a proxy for atmospheric soot a σ_a value of 4 $m^2\ g^{-1}$ at $\lambda = 670$ nm was determined by laser transmission measurements of particle loaden filter samples (Petzold et al., 1997). More recently, lower σ_a values of this type of soot were determined by using an integrating sphere (2.9 ± 0.1 @ $\lambda = 550$ nm; Ballach, Hitzenberger, Schultz, & Jaeschke, 2001) as well as by photoacoustic measurements (2.7 ± 0.1 @ $\lambda = 680$ nm; Krämer, Bozoki, & Niessner, 2001). The strong variability of σ_a between 5 and 20 $m^2\ g^{-1}$ measured for ambient aerosol samples by the corresponding aethalometer method was explained entirely by the physical and chemical variability of the soot in relation to the combustion origin and the degree of atmospheric aging (Liousse et al., 1993). In this method the absorption coefficient is related to the light absorbing mass content (black carbon, BC) of the aerosol which is usually equated to the elemental carbon mass content EC (for details see Saathoff et al., 2003b). Using the integrating plate method Horvath (1995) measured σ_a values around 10 $m^2\ g^{-1}$ ($\lambda = 550$ nm) for flame soot and soot originating from Diesel engine exhaust. The absorption cross section of pure airborne combustion soot was investigated by Colbeck, Atkinson, and Johar (1997) and Dobbins et al. (1994) by closure between the extinction and scattering coefficients b_e and b_s measured simultaneously at $\lambda = 632$ nm. They found σ_a values between 6.0 and 8.1 $m^2\ g^{-1}$ depending only slightly on the type of hydrocarbon fuel and the size of the soot aggregates. Thus, comparing all these experiments there is evidence for a difference in σ_a between spark discharge soot and atmospheric soot emitted by fuel combustion.

The integrating plate method (IPM) is a very simple and frequently used method to measure directly the absorption coefficient b_a of atmospheric aerosols deposited on filters (Horvath, 1995). Horvath (1997) investigated the systematic errors of the IPM induced by the diffuse scattering of the filter substrate and the multiple scattering within the deposited aerosol sample. He found absorption coefficients which are always higher than the true value determined independently on airborne particles by closure between extinction and scattering coefficient, b_e and b_s. The deviation was found to be dependent mainly on the absorption-to-extinction ratio b_a/b_e determined by the independent subtraction method. From this laboratory investigation on aerosols with different mixing states between carbon and a purely scattering component, a calibration function was determined to correct the IPM absorption coefficient. For pure carbon aerosol a minimum correction factor of 1.24 was determined whereas the factor reaches 4.5 for very weakly absorbing aerosol. Filter samples were prepared for the IPM during the AIDA Soot Aerosol Campaign 1999 to check the quality of this calibration for model aerosols which are more related to the atmospheric aerosol.

1.4. Atmospheric processing of soot

During the residence times of atmospheric aerosols in the tropospheric boundary layer from days to weeks their compositions and size distributions are changed mainly due to nucleation scavenging

and coagulation (Raes et al., 2000). This processing also results in a change of the aerosol optical properties. E.g. the transition from external to internal mixing of soot with sulfate aerosol may lead to an enhancement of soot mass specific absorption cross section σ_a. In this respect, two types of mixing, heterocoagulation of dry particles or uptake of soot into deliquescent sulfate particles have been investigated theoretically (Fuller et al., 1999). They found a maximum enhancement in σ_a of soot aggregates around 30% by adhesion to spherical sulfate particles for $\lambda = 550$ nm. More significantly, encapsulating a single carbon sphere by a spherical dielectric host, e.g. ammonium sulfate, leads to an absorption increase by a factor of 2 compared to the isolated carbon particle. Furthermore, soot particles may act as condensation nuclei for atmospheric oxidation products of volatile organics. This coating changes the hygroscopic as well as the optical properties of the soot particles significantly.

We present and discuss in this paper the results of the optical measurements which we performed during the extensive AIDA Soot Aerosol Campaign 1999. Emphasis is given to the delivery of detailed aerosol optical properties over the visible spectral region which are necessary for a more realistic modeling of the impact of anthropogenic soot emissions on visibility and climate.

2. Experimental

The aerosol chamber AIDA and the course of the experiments are described in detail in the introduction paper (Saathoff et al., 2003a). For the characterization of the aerosol optical properties the following experimental devices were used: (1) flow tube extinction spectrometer to acquire UV-VIS-NIR extinction spectra in the 230–1000 nm region, (2) folded path extinction cell (75 m, White type) to measure sensitively the extinction coefficient at 473 nm with a spectral bandwidth of 35 nm, (3) three color integrating nephelometer (TSI, model 3563) to measure the scattering coefficients and backscatter ratios at 450, 550, and 700 nm, (4) integrating plate to determine directly the absorption coefficients at 450, 550, and 650 nm on filter samples. The flow tube extinction spectrometer consists of a flow tube of ~5 m length and 40 mm inner diameter which is used as an optical cell. The system is equipped with a deuterium/halogen lamp combination (Avantes, model DH-2000-FHS) and quartz fiber optics. The lamp combination has a total power of ~100 W and an emission range from 215 to 1500 nm. Bundles composed of 20 step index quartz/quartz fibers each having a diameter of ~100 μm, a numerical aperture of 0.22, and a length of 4 m are used as light guides. Due to damaging by the UV-C (< 280 nm) light emission of the deuterium lamp the fiber transmission decreases very rapidly for wavelengths below 230 nm leading to an induced damping for this spectral region of more than 10 dB m^{-1} after a few hours of irradiation (Klein et al., 1997). This solarization effect is the reason why the system is limited to wavelengths longer than 230 nm. A collimated light beam along the axis of the flow tube is achieved by 90°C off-axis parabola aluminum mirrors. The transmitted light is analyzed by a diode array spectrometer (Zeiss, model MCS 55) with a sensitivity of 15 bit, a spectral resolution of 2.5 nm, and a spectral range from 190 to 1015 nm. The light source was monitored simultaneously with a second identical spectrometer, which provides the correction of possible lamp drifts during the measurement. The system has a physical detection limit of $\sim 10^{-4}$ m^{-1} in the wavelength range from 230 to 900 nm. The flow tube spectrometer was run in series with the folded path optical cell and the nephelometer (Fig. 1). Thus, absorption coefficients b_a at 450, 500, and 700 nm could be determined by closure between b_e and

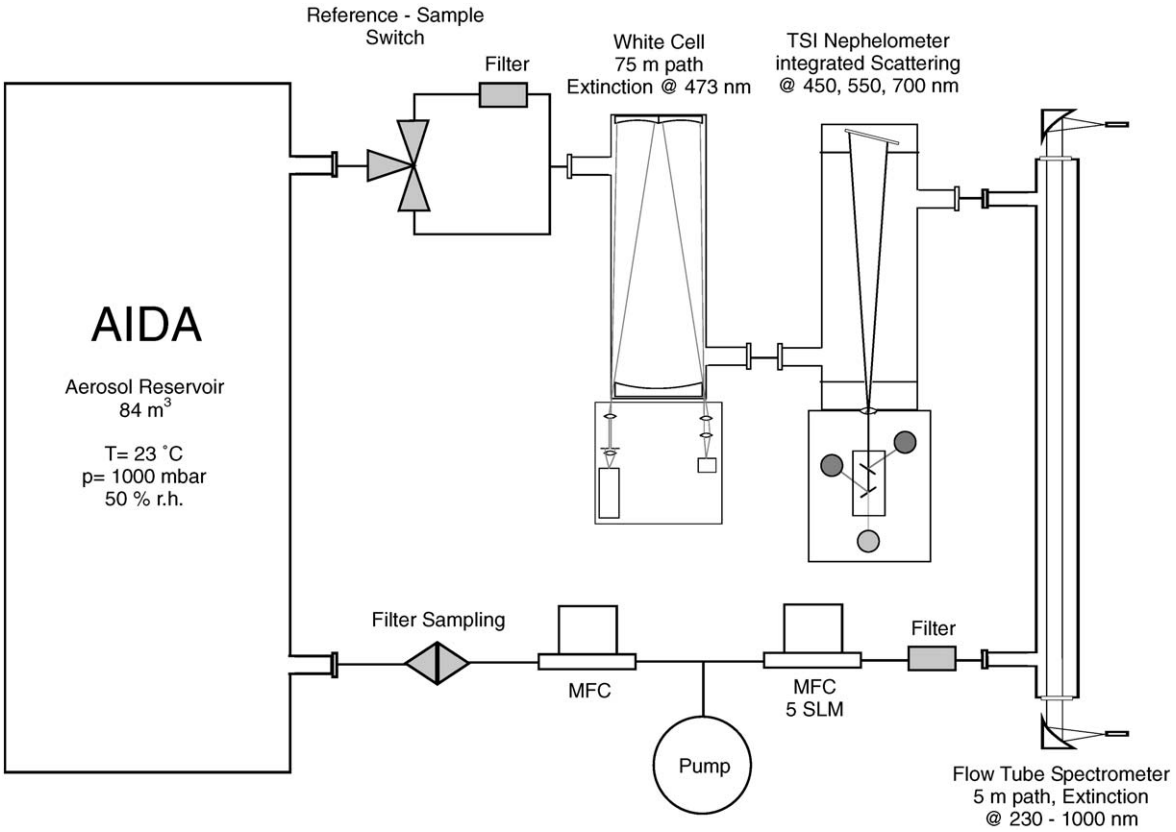

Fig. 1. Experimental set up used to measure aerosol optical properties.

b_s (difference method, DM) and thus single scattering albedos ω_0 could be determined for these wavelengths as well. Particle free and particle containing air from the AIDA chamber was pumped periodically through the system with a controlled flow of 5 SLM. This experimental course provides reference–sample–reference cycles with a duration of ~30 min.

The integrating plate method (IPM) is described in detail elsewhere (Horvath, 1997). Here, only the basic philosophy of this method is given. The light transmitted through an opaque filter is measured by a photo multiplier. By installing an opal glass plate between the filter and the photo multiplier not only the directly transmitted light is collected but also light scattered diffusely by the filter as well as by the deposited aerosol. Thus, by assuming that all scattered light is measured (integrated), the transmission loss of a particle loaden filter can be assigned to absorption by the particles. For each experiment we sampled at least one Nuclepore filter for the IPM analysis which were performed at the University of Vienna.

The temporal evolution of the particle concentration and the particle size distribution during the experiments of duration up to two days was monitored by a condensation nuclei counter (CNC, TSI, model 3022A) and a scanning mobility particle sizer (SMPS, TSI, DMA model 3932 in combination with CNC model 3010). The total carbon mass concentration (TC) was determined by CO_2-coulometry of filter samples and online photoacoustic soot monitoring. The sulfate mass

concentration was determined by ion chromatography of filter samples and in situ FTIR absorption spectroscopy. For details concerning the sensitivity and accuracy of these methods see Saathoff et al. (2003b). Based on these analysis of the aerosol mass concentrations, mass specific cross sections were deduced from the extinction, scattering, and absorption coefficients.

3. Modeling

Time evolution of particle mass and number concentration of soot aerosol were modeled by the COSIMA code, which simulates the dynamics of agglomerate aerosol particles on the basis of fractal scaling laws (Naumann, 2003). The code has been updated recently by implementing an optics module that allows to predict the time evolution of σ_e and σ_s in the presence of coagulation and to extract information on the complex refractive index from respective measurements. The module was developed within the framework of the Rayleigh–Debye–Gans (RDG) approximation which implies the neglect of multiple scattering and self interactions within a fractal-like aggregate. Under these assumptions the mass-specific absorption cross section σ_a of an aggregate is independent of size and is equal to the cross sections of the individual particles σ_a^p:

$$\sigma_a = \sigma_a^p. \tag{1}$$

For primary particle sizes within the Rayleigh limit ($x_p \ll 1$) Mie-theory is reduced to the electrostatic limit (Bohren & Huffman, 1983), and the monomer absorption cross section is expressed by

$$\sigma_a^p = \frac{6\pi}{\lambda\rho}\,\mathrm{Im}\left\{\frac{m^2-1}{m^2+2}\right\}, \tag{2}$$

with ρ the density and $m = n + ik$ the complex refractive index of the soot material. Thus, σ_a of fractal soot aggregates is dominated mainly by the refractive index of the soot material and is independent of the monomer and aggregate size. The wavelength dependence of σ_a and σ_s is usually described by a power law $\sigma \sim \lambda^{-\alpha}$ with α the Ångström exponent. If $(m^2-1)/(m^2+2)$ in Eq. (2) is only a weak function of wavelength an Ångstrom exponent close to 1 is expected from the RDG approximation.

Within the RDG approximation, σ_s of an ensemble of large polydisperse aggregates shows an asymptotical behavior with aggregate size (for details see Naumann, 2003). Here, the result of σ_s for the case of an ensemble of large monodisperse aggregates is given for simplicity (Dobbins et al., 1994):

$$\sigma_s = \sigma_s^p k_f \left(\frac{3D_f}{16x_p^2}\right)^{D_f/2}. \tag{3}$$

Thus, σ_s is proportional to the cross section σ_s^p of the individual particles scaled by a structure factor which is dependent only on the fractal parameters k_f, the volume filling factor, and D_f, the fractal dimension, and which is independent of the actual aggregate size. In the Rayleigh limit the scattering cross section of the primaries is expressed by

$$\sigma_s^p = \frac{4\pi x_p^3}{\lambda\rho}\left|\frac{m^2-1}{m^2+2}\right|^2. \tag{4}$$

If $(m^2-1)/(m^2+2)$ in Eq. (4) is a weak function of wavelength and assuming a fractal dimension $D_f = 2$ an Ångström exponent close to 2 is expected from Eqs. (3) and (4).

It has been shown by comparison with a more general integral formulation that the error in σ_a and σ_s introduced by the RDG approximation remains below 10% as long as the size parameter of the soot primaries satisfies the condition $x_p < 0.3$ (Farias, Köylü, & Carvalho, 1996). For Diesel and spark discharge soot this condition is well fulfilled over the spectral range of interest, as we will see in the following section.

4. Results and discussion

A general overview of the experiments including their numeration is given by Saathoff et al. (2003a). The main aim of the AIDA Soot Aerosol Campaign 1999 was an extensive comparison of the physical and chemical properties of Diesel (VW, TDI 1.9 L) and spark discharge (Palas, model GfG 1000) soot aerosol. Thus, we present and discuss the results of experiment # 2 (pure Diesel soot) and experiment #3 (pure spark generated soot). The optical properties of pure ammonium sulfate aerosol are based on an additional experiment performed after the campaign. From the mixing and coating experiments we present the results of experiment # 6 (Diesel soot/ammonium sulfate) and experiment #9 (coating of spark generated soot with secondary organic material).

4.1. Comparison of the optical properties of Diesel and spark discharge soot

A comparison of the mass specific extinction spectra and absorption cross sections of Diesel and spark discharge soot is given in Fig. 2. The characteristic spectral properties of the two soot types are compared in Table 1. These results are mean values deduced from experiments #2 and #7 in case of Diesel and from experiments #3 and #9 in case of spark discharge soot. The fractal parameters deduced from the analysis of the coagulation dynamics of experiment #2 and #3 by means of the COSIMA model are given in Table 2. It was found that the particles of the two soot types do not differ in the aggregate fractal dimension, but differ significantly in the primary particle size in agreement with the HRTEM analysis (Wentzel et al., 2003).

At $\lambda = 473$ nm the σ_e spectra are in good agreement with the corresponding σ_e values measured by the white-cell indicating that mass losses within the system can be neglected in case of soot. The wavelength dependence of σ_e is typical for soot with a steep rise towards the UV and a maximum in the mid-UV between 200 and 260 nm. As already mentioned this broad extinction (absorption) band is usually attributed to an interband π–π^* transition within the electronic density of states of the disordered soot structure. The maximum of this transition is found at 250 nm for Diesel soot and at $\leqslant 230$ nm in the case of spark generated soot (a value of 220 nm was determined in subsequent measurements with an UV-extended measurement range).

It is clear from Fig. 2 that the optical properties of Diesel soot differ significantly from those of spark generated soot. Especially the difference in the absolute values of σ_e and the different band positions are eye-catching. The difference in σ_e is mainly due to the higher absorption efficiency of Diesel soot, which exceeds σ_a of spark discharge soot by a factor of two in the visible. Here, it is important to note that the difference in σ_a is less but still significant when relating the absorption coefficient to the EC mass fraction of the corresponding soot type. This is due to the low EC content

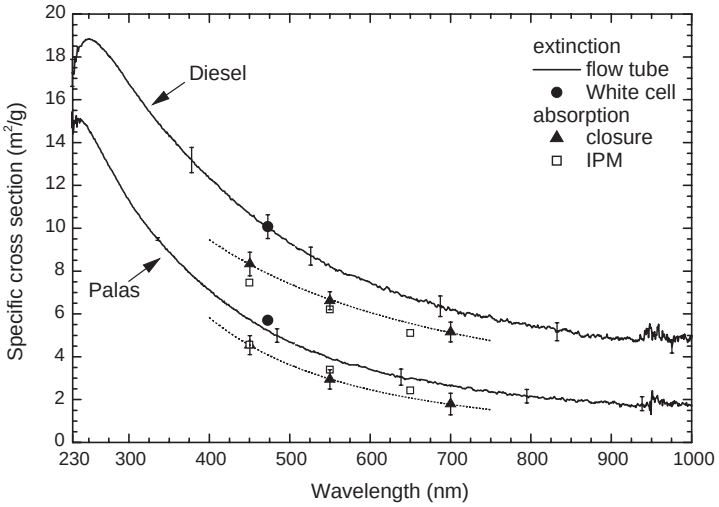

Fig. 2. Comparison of the mass specific absorption and extinction cross sections of spark discharge (Palas) and Diesel soot. Solid lines: spectrally resolved extinction cross sections measured by the flow tube spectrometer. Circles: monochromatic extinction cross section at $\lambda = 473$ nm measured by the extinction cell. Filled triangles up and dotted lines: absorption cross sections at $\lambda = 450$, 550, and 700 nm determined by closure with scattering coefficients measured by the nephelometer. The absorption cross sections deduced by the integrating plate method (IPM) at $\lambda = 450$, 550, and 650 nm are shown for comparison.

of 60% determined for spark discharge soot. Since this soot is formed in pure argon atmosphere, the low EC content of the thermal analysis is obviously not a result of a significant amount of "organic" carbon in the particles but reflects the specific bonding structure of this type of soot (see Saathoff et al., 2003b).

However, the difference in σ_a is not spectrally independent but decreases with decreasing wavelength, reflected by the two times higher absorption Ångström exponent α_a of spark generated soot (Table 1). These exponents were deduced by fitting the respective absorption data by a power law as $\sigma_a \sim \lambda^{-\alpha}$. As was discussed above, an Ångström exponent close to 1 is expected in spectral regions where the refractive index of the particle material has a weak spectral dependence and the particle size is much smaller than the wavelength of light ($x_p \ll 1$). The exponents $\alpha_a = 1.1$ and $\alpha_s = 1.9$ found for Diesel soot are comparable to the expected values and, therefore, point towards a weak wavelength dependence of the corresponding refractive index. In case of spark discharge soot a much stronger wavelength dependence of the refractive index is expected from the Ångström exponents given in Table 1.

Since the size parameter of the primaries of both soot types are well within the Rayleigh regime in the visible spectral region (Table 2), the observed differences in σ_a, α_a, and α_s can only be explained in terms of distinct refractive indices, i.e. distinct solid state structures of the two soot types. Based on the fractal parameters given in Table 2, the RDG analysis of the initial measurements of σ_e, σ_s and the size distribution of experiments #2 and #3 indeed yield refractive indices which differ significantly (Table 3), but are within the range of values reported by Fuller et al. (1999).

This interpretation is supported by the observation of different wavelength positions of the π–π^* band maximum. According to the BSU model of disordered soot material, the band position in the

Table 1
Comparison of the mean spectral optical properties of Palas and Diesel soot. 1σ standard deviations are given as statistical errors. A wavelength dependent systematic error are taken into account in the scattering coefficients

Spectral property	Palas soot	Diesel soot
σ_e ($\lambda = 450$ nm)	5.7 ± 0.3 m^2 g^{-1}	10.6 ± 0.5 m^2 g^{-1}
σ_s ($\lambda = 450$ nm)	$1.2 + 0.3 - 0.2$ m^2 g^{-1}	$2.3 + 0.3 - 0.1$ m^2 g^{-1}
σ_a ($\lambda = 450$ nm)	$4.5 + 0.3 - 0.4$ m^2 g^{-1}	$8.3 + 0.5 - 0.7$ m^2 g^{-1}
ω_0 ($\lambda = 450$ nm)	0.21 ± 0.03	0.22 ± 0.01
σ_e ($\lambda = 550$ nm)	3.9 ± 0.4 m^2 g^{-1}	8.2 ± 0.4 m^2 g^{-1}
σ_s ($\lambda = 550$ nm)	$1.0 + 0.2 - 0.1$ m^2 g^{-1}	1.6 ± 0.2 m^2 g^{-1}
σ_a ($\lambda = 550$ nm)	$2.9 + 0.4 - 0.5$ m^2 g^{-1}	6.6 ± 0.4 m^2 g^{-1}
ω_0 ($\lambda = 550$ nm)	0.25 ± 0.04	0.20 ± 0.01
σ_e ($\lambda = 700$ nm)	2.6 ± 0.4 m^2 g^{-1}	6.2 ± 0.3 m^2 g^{-1}
σ_s ($\lambda = 700$ nm)	0.8 ± 0.2 m^2 g^{-1}	1.0 ± 0.1 m^2 g^{-1}
σ_a ($\lambda = 700$ nm)	$1.8 + 0.4 - 0.5$ m^2 g^{-1}	5.2 ± 0.3 m^2 g^{-1}
ω_0 ($\lambda = 700$ nm)	0.28 ± 0.05	0.17 ± 0.01
α_a ($\lambda = 450$–700 nm)	2.1	1.1
α_s ($\lambda = 450$–700 nm)	0.9	1.9
π–π^* band position	220 nm	250 nm

Table 2
Fractal parameters deduced by modeling the coagulation dynamics of experiment #2 and #3 by means of the COSIMA model

Parameter	Palas soot	Diesel soot
fractal dimension D_f	2.0	2.0
prefactor k_f	5.6	5.6
primary particle size d_p	7 nm	27 nm
size parameter x_p @ 550 nm	0.04	0.15
primary particle density ρ	2.0 g cm^{-3}	1.7 g cm^{-3}

200–260 nm spectral region is sensitive to the BSU size in a way that the larger the microcrystallites the longer the wavelength of the band position. As already mentioned, Jäger et al. (1999) found a band position around 220 nm for soot material with no detectable BSU structure whereas a band position around 265 nm was reported for a soot material with a BSU structure clearly detectable by HRTEM analysis. In the HRTEM analysis of our soot samples a BSU structure was observed in case of Diesel soot, whereas for spark generated soot structural order could be detected only in rare cases (Wentzel et al., 2003). Following this study the Diesel soot monomers consist of BSUs of stacked 7-10 graphite (002) layers in a concentrical arrangement. Altogether, the comparison of the

Table 3
Complex refractive index $m=n+ik$ deduced by the RDG analysis of the initial extinction, absorption coefficients and size distributions of experiment #2 and #3 and based on the COSIMA model results given in Table 2

Wavelength	Palas soot	Diesel soot
450 nm	2.18 + i 0.94	1.41 + i 0.64
550 nm	2.65 + i 1.32	1.49 + i 0.67
700 nm	—	1.57 + i 0.73

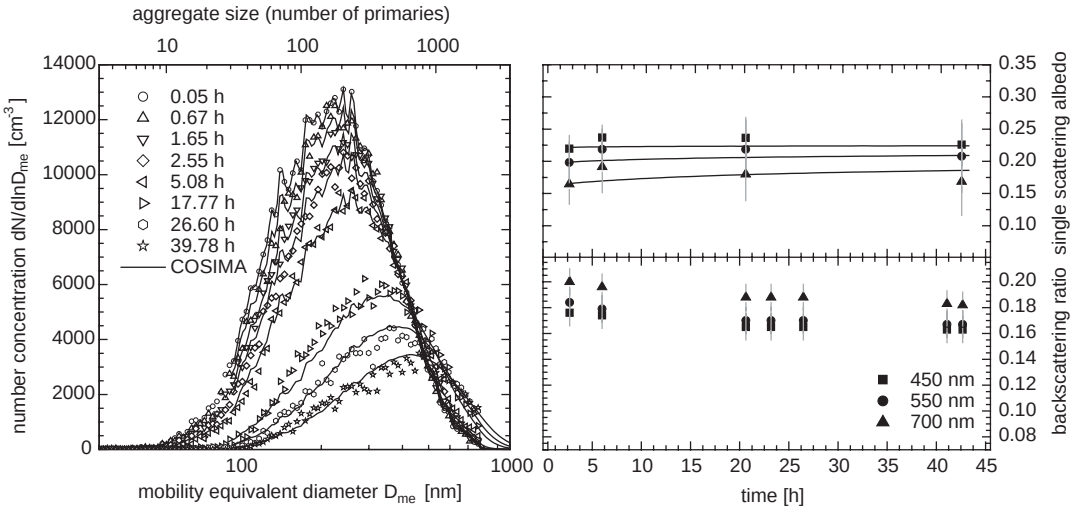

Fig. 3. Time evolution of the Diesel soot size distribution and the corresponding scattering properties at the three nephelometer wavelengths during experiment #2. The solid lines in the plots represent model results by COSIMA.

spectral optical properties of Diesel and spark discharge soot reveals different solid state structures in good agreement with the structural analysis by HRTEM.

The specific absorption cross sections σ_a determined by closure are in good agreement with the values deduced from the absorption coefficients measured by the IPM. A more thorough comparison of the results gained by the two methods during the campaign is given at the end of this section.

4.2. The influence of coagulation on the optical properties of soot

The temporal evolution of the particle size distribution, the single scattering albedo ω_0, and the backscattering ratio of pure Diesel soot in the visible are shown in Fig. 3 for experiment #2. The initial carbon mass and particle number concentrations were 67 μg m^{-3} and 1.9×10^4 cm^{-3} in this experiment. From the initial size distribution, number concentration, and mass concentration a volume fractal dimension of $D_f=2$ and a primary particle diameter of $d_p=27$ nm follows from the COSIMA

model (Table 2). Very good agreement between the measured and simulated size distributions was achieved on the experimental time scale. Coagulation-induced aggregate growth is reflected by the time evolution of the size distribution, starting from a mean mobility equivalent diameter of ~250 nm to a diameter of ~500 nm after aging the aerosol for 44 hours. Based on the COSIMA model this growth in mobility equivalent diameter corresponds to an increase of the mean number of primaries per aggregate from ~200 to more than 600. Within the experimental accuracy and except for the first few hours, ω_0 and the hemispheric backscattering ratio did not change significantly with the ongoing coagulation-induced particle growth. Note the relatively high scattering albedo of about 0.20 and the low backscattering ratio of about 0.17 compared to $\omega_0 < 0.01$ and a backscattering ratio of ~0.5 calculated for the primary particles by Mie theory using the corresponding refractive index of Table 3.

Following Naumann (2003) the RDG approximation predicts an asymptotical behavior of σ_s and, hence, of the single scattering albedo ω_0 with aggregate size. As discussed in the previous section the refractive index of the soot material at 450, 550, and 700 nm was deduced from the initial size distribution. Based on this refractive index, the time evolution of ω_0 was calculated with the COSIMA model by applying the RDG approximation. The results are compared in Fig. 3 with the experimental data. Thus, the observed near constancy of ω_0 on the experimental time scale can be explained as a result of the fractal nature of the soot particles and the conservation of their fractal dimension during the coagulation process. From Fig. 3 a tendency of the experimentally determined ω_0 to decrease with time is not predicted by the model. Here one has to keep in mind that due to technical restrictions the nephelometer has blind spots at small (0–7°) and large (170–180°) scattering angles leading to measured scattering coefficients which are systematically too small, for particles exceeding the Rayleigh limit. It can be shown by using a more sophisticated T-matrix model for light scattering by fractal particles that this effect introduces a systematic error of the order of 5–10% for aggregates composed of 500 to 1000 primaries and, thus, might be responsible for the gradual decrease of ω_0 in Fig. 3.

In Fig. 4 the temporal evolution of the aggregate size distribution of pure spark discharge soot and the corresponding scattering properties are plotted for experiment #3. The initial carbon mass and particle number concentrations were 100 μg m^{-3} and 1.5×10^5 cm^{-3} in this experiment. Due to the higher particle number concentration compared to experiment #2 the coagulation time scale is shorter in this experiment leading to a much faster aggregate growth reflected by the temporal evolution of the size distribution in Fig. 4. A corresponding mean aggregate growth from 1700 to more than 10000 primaries per aggregate was calculated from the mobility equivalent diameter using the COSIMA parameterization (Table 2). This fast coagulational growth is the reason for the significant increase of the single scattering albedo during the first 20 h. Note the smaller backscattering ratio of spark discharge soot compared to the ratio measured for Diesel soot. Since the scattering asymmetry is determined by the aggregate size (e.g. Sorensen et al., 1992), this difference reflects the difference in monomers per aggregate which is of the order of one magnitude between Diesel and spark discharge soot.

4.3. Dry ammonium sulfate aerosol

The pure ammonium sulfate aerosol experiment (experiment #4) was performed as a reference for the subsequent mixing experiments with Diesel soot. The experiment was performed at ~50%

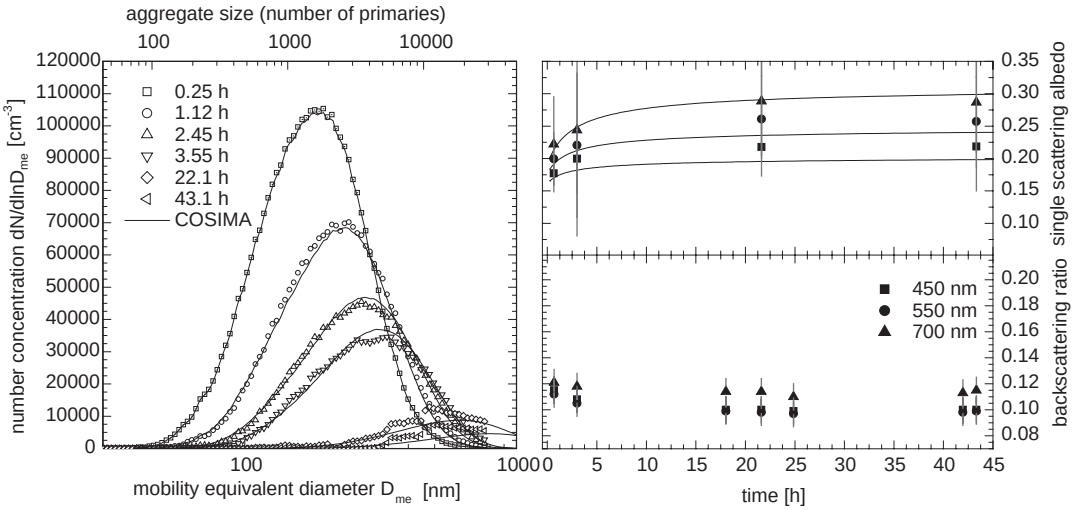

Fig. 4. Same as Fig. 3 but for Palas soot, experiment #3.

r.h. which is well below the deliquescence humidity of 80% r.h. of the initially dry $(NH_4)_2SO_4$ aerosol. Thus, the sulfate particles remained solid during the entire experiment. For the analysis of the mixing experiments the temporal behavior of the $(NH_4)_2SO_4$ specific scattering cross section σ_s is required in more detail than delivered by experiment #4. Therefore, an additional experiment with dry ammonium sulfate aerosol was performed under comparable conditions after the campaign to determine the temporal behavior of σ_s more accurately. This was achieved by collecting filter samples simultaneously with the optical measurements for mass analysis by ion chromatography. The initial $(NH_4)_2SO_4$ number and mass concentrations were 25000 cm^{-3} and 505 μg m^{-3} in this experiment. On the experimental time scale of 37 h the volume size distribution is shifted and broadened due to coagulation, starting from an initial mass median diameter of 350–440 nm at the end of the experiment (Fig. 5). Since we used a cyclon impactor to prevent larger particles from reaching the chamber the initial size distribution had a narrow width of $\sigma = 1.26$. Due to sampling as well as sedimentational and diffusional losses the mass concentration decreased during the experiment to a value of 280 μg m^{-3} at the end of the experiment. This is well reflected by the temporal decrease of the extinction coefficient spectra in Fig. 6. By using UV-stabilized fibers in this experiment the measurement range could be extended down to 200 nm. A single scattering albedo close to 1 was deduced from the extinction and scattering measurements at 450, 550, and 700 nm as expected for dry $(NH_4)_2SO_4$ which does not absorb in this wavelength range ($n = 1.54$–1.52 and $k \approx 10^{-7}$, Toon, Pollack, & Khare, 1976). The extinction spectra possess a wavelength dependence typical for non-absorbing Mie-type scatterers, with an Ångström exponent of $\alpha_s \approx 2$ for the cross section increase towards the UV leading to a reddening of transmitted white light. Another characteristic extinction feature is the maximum in the near-UV which is interpreted as the interference between the incident and forward-scattered (refracted) light. On the blue side of the extinction peak a steep decrease of the extinction coefficient towards the mid-UV is observed in the initial spectrum in Fig. 6. As part of the interference structure of monodisperse spherical particles, which tends to vanish as the dispersion of the particle radii increase, this “bluing” effect indicates that the initial

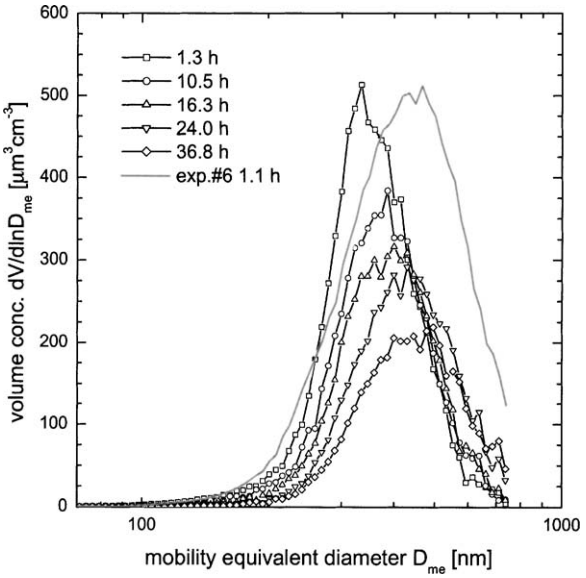

Fig. 5. Time evolution of the ammonium sulfate volume size distribution. The initial distribution of experiment #6 is plotted for comparison. Note that this distribution is plotted in arbitrary units, normalized to the same peak height. Note also that in contradiction to Figs. 3 and 4 the solid lines do not represent COSIMA results but just interpolate the data points.

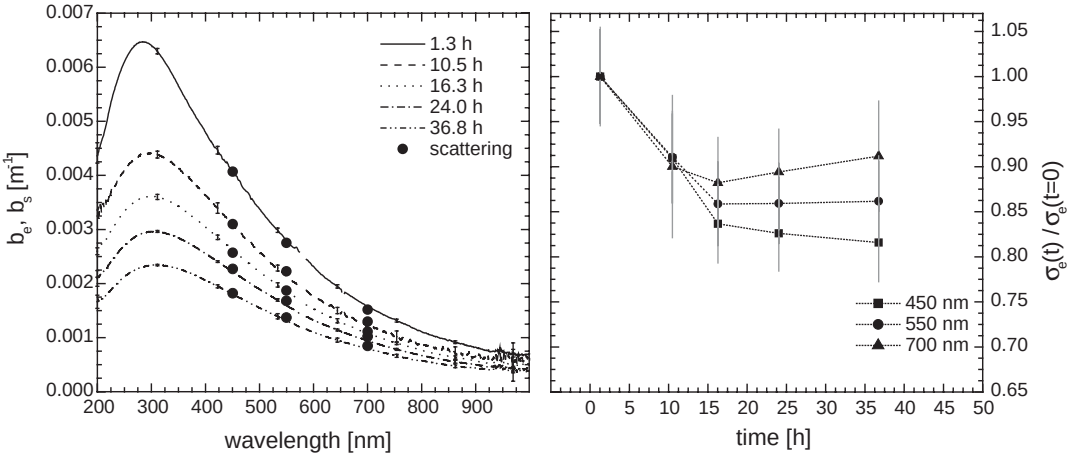

Fig. 6. Time evolution of the ammonium sulfate extinction coefficient (left) and the mass specific extinction cross sections relative to the initial value (right). The extinction or scattering cross sections in the visible are decreasing due to coagulation within the first 15 h after aerosol addition.

size distribution indeed had a small width. The particle coagulation in the chamber is reflected by the gradual broadening and red-shift of the interference maximum.

Now, for the interpretation of the subsequent results in case of externally and internally mixed soot/sulfate aerosol it is important to note that the mass specific scattering (or extinction) cross

section in the visible is not constant but decreases with the ongoing particle coagulation within the first 15 h. This can be shown by plotting in Fig. 6 σ_e at different times relative to the initial value. Thus, a decrease in σ_e (or σ_s) of up to 20% can be expected by coagulation of sulfate aerosol depending on the initial number concentration and the wavelength of light. For the initial size distribution of Fig. 5 we deduced specific cross sections at 450, 550 and 700 nm of 7.9 ± 0.4, 5.5 ± 0.3 and 3.1 ± 0.2 m^2 g^{-1}, respectively.

4.4. The influence of heterocoagulation with $(NH_4)_2SO_4$ aerosol on the optical properties of Diesel soot aerosol

To investigate the effect of heterocoagulation on the optical properties of Diesel soot, an ammonium sulfate/Diesel soot aerosol, externally mixed at the beginning, was studied for 2 days in experiment #6. The initial mass concentrations were 1500 μg m^{-3} ammonium sulfate and 93 μg m^{-3} Diesel soot. Mass concentrations of 700 g m^{-3} $(NH_4)_2SO_4$ and 66 μg m^{-3} soot were determined after 43 h. For details concerning the determination of the mass concentrations and their temporal evolution during the experiment see Saathoff et al. (2003b).

The initial sulfate number concentration was 48000 cm^{-3} which is roughly a factor of 2 higher than the concentration in the reference experiment. Since no cyclon impactor was used in this experiment the initial size distribution of the ammonium sulfate aerosol has a larger mass median diameter of 426 nm and width of $\sigma = 1.41$ compared to the distribution of the reference experiment (Fig. 5). A qualitative analysis of the aerosol mixing state with time was performed by transmission electron microscopy (Wentzel et al., 2003) as well as by single particle mass spectroscopy (Kirchner, Vogt, Natzeck, & Goschnik, 2003). Both methods clearly showed an increase of the relative abundance of internally mixed aerosol particles with experimental time. A maximum relative abundance of internally mixed particles of ten to twenty percent was estimated in these studies, showing that a complete internal mixture was certainly not reached during the experiment.

The temporal evolution of the extinction spectra and the b_a/b_s ratio at $\lambda = 450$ nm is plotted in Fig. 7. Due to the different optical properties of the two aerosols the absorption coefficient is entirely dominated by soot whereas at the given mass ratio the scattering coefficient is dominated by sulfate. Thus, the absorption-to-scattering ratio b_a/b_s reflects the relative change of the cross sections of the two aerosol types due to coagulation. In the previous section it was shown that σ_s of the sulfate aerosol decreases due to coagulation. To derive the influence of heterocoagulation on the absorption cross section of soot the b_a/b_s ratio was corrected to account for the effect of coagulation between sulfate particles on b_s. The remaining increase in b_a/b_s is then due to the different lifetimes of sulfate and soot particles in the chamber, reflected by the changing mass ratio, plus a possible soot absorption enhancement due to heterocoagulation with sulfate. According to the filter analysis the soot/sulfate mass ratio increased by a factor of 1.5 within 43 h whereas the corrected b_a/b_s ratio at 450 nm increased by a factor of 1.8 during the same time. The remaining absorption enhancement factor of 1.2 might be due to heterocoagulation of Diesel soot with sulfate aerosol. As already mentioned in the introduction Fuller et al. (1999) have investigated theoretically the absorption enhancement of spherical soot particles by adhesion to dry ammonium sulfate particles. They found an absorption enhancement which tends to increase with the mean size of the sulfate particles, increasing k values of the soot refractive index, and decreasing size of carbon particles. A maximum enhancement factor of 1.38 was reported assuming single spherical soot particles of 20 nm diameter sticking to the surfaces

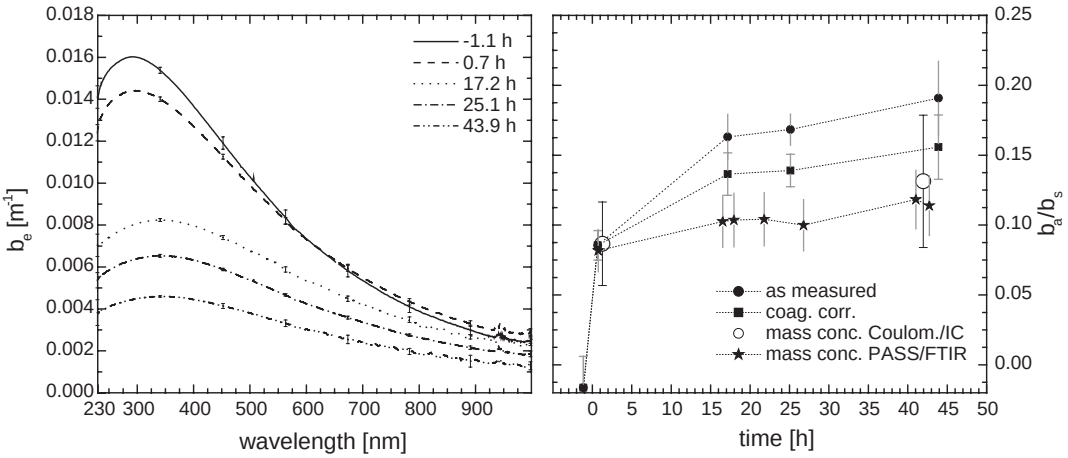

Fig. 7. Temporal evolution of the extinction coefficient (left) and the absorption-to-scattering ratio b_a/b_s (right). The values at negative times refer to the pure ammonium sulfate aerosol. The time origin denotes the end of the soot admixing process. The ratio was corrected for the coagulation-induced change of the sulfate scattering cross section (Fig. 6). The large open circles represent b_a/b_s values expected from the filter-based mass ratio only, e.g. ignoring changes in the aerosol cross sections by coagulation. The same holds for the b_a/b_s values determined from the mass concentrations measured by the photoacoustic soot sensor and deduced from the infrared sulfate spectra (stars).

of log-normally distributed sulfate particles. The count mean diameter of the sulfate distribution was 200 nm and a refractive index of $m = 2.0 + i$ was assumed for the soot material. Although this result might be sufficient to explain the enhancement found in experiment # 6, the computations with parameters more comparable to the experiment yield an absorption enhancement factor of only 1.04. These enhancement values agree quite well with own computations using the multiple sphere code developed by D. Mackowski, K. Fuller, and M. Mishchenko (Mackowski, 1994), which is publicly available. By assuming a reasonable agglomerate configuration and using the agglomerate parameters and refractive index deduced from the pure Diesel soot experiment (Tables 2 and 3) the calculations yield an absorption enhancement factor at $\lambda = 450$ nm of 1.04 for a soot aggregate in the vicinity of a dry ammonium sulfate sphere of 285 nm in diameter. Keeping in mind that the mixing state was far from complete one can conclude that the observed enhancement factor is likely due to the insufficient correction of the sulfate scattering cross section rather than caused by a soot absorption enhancement. Reasons for that might be the higher number concentration and the larger mass median particle size and distribution width of the sulfate aerosol compared to the reference experiment (Fig. 5). This conclusion is further supported by the temporal evolution of the soot/sulfate mass ratio deduced independently from the photo acoustic soot signal, i.e. the soot absorption cross section at λ=680 nm and the infrared sulfate absorption spectra. At t=43 h this ratio agrees quite well with the soot/sulfate mass ratio deduced by the filter analysis. Thus, within the experimental uncertainties the mean specific soot absorption cross section of the mixed soot/sulfate aerosol ensemble is not affected by that part of the aerosol which forms an internal mixture. This means in turn that the enhancement factor of the Diesel soot absorption cross section in an internal mixture with dry ammonium sulfate aerosol does not differ significantly from the value of 1.04 predicted by the simulations.

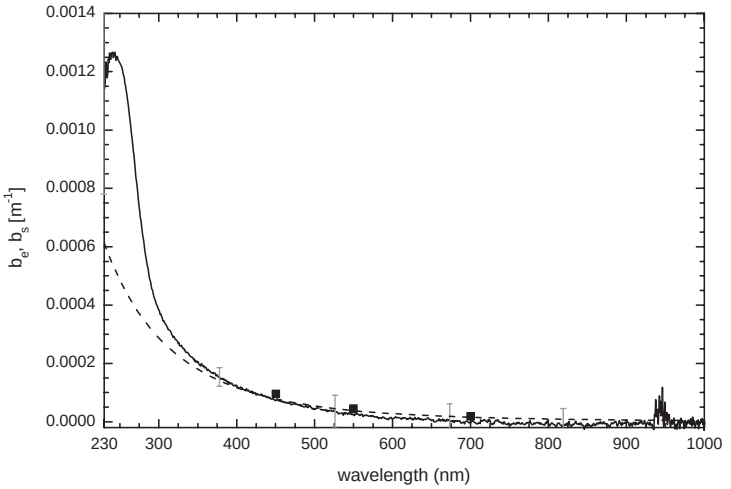

Fig. 8. Extinction spectrum of homogeneously nucleated SOA measured 1.33 h after admixing α-pinene (solid line). The squares represent the scattering coefficients measured by the nephelometer. The dashed line gives the result of a Mie calculation using the experimental size distribution at 1.23 h as input and assuming a wavelength independent real refractive index $n = 1.44$. The absorption below 350 nm is partially due to ozone, see text.

4.5. Coating of spark generated soot with secondary organic aerosol (SOA) mass

Three coating experiments were carried out during the AIDA Soot Aerosol Campaign 1999. In experiment #7 the chamber was filled with Diesel soot, in experiment #8 with ammonium sulfate, and with spark discharge soot in experiment #9 (Saathoff et al., 2003a). Here, we discuss the results of experiment #9 in detail whereas a general overview of the coating experiments and their results is given by Saathoff et al. (2003c).

We generated SOA in situ by admixing 470 ppb ozone to the chamber, followed by the addition of 61 ppb (343 μg m^{-3}) α-pinene vapor. Using the product yield data determined from the homogeneous SOA nucleation experiment #10, the maximum SOA mass density resulting from the ozonolysis of 343 μg m^{-3} α-pinene in our chamber should be 65 μg m^{-3} (Saathoff et al., 2003c). The density ρ and real refractive index n of the SOA are not known, but may be estimated by comparison with similar compounds for which these data are available, e.g. pinic acid diethyl ester with $\rho = 1.0104$ g cm^{-3} and $n = 1.4496$, or cyclopropanedicaboxylic acid diethyl ester with $\rho = 1.062$ g cm^{-3}, $n = 1.445$, or octanedioic acid diethyl ester with $\rho = 0.9811$ g cm^{-3}, $n = 1.433$ ($\lambda = 589$ nm; Lide, 1999).

Because the optical properties of the SOA substance resulting from the ozonolysis of α-pinene are unknown in the wavelength range of our study, we have generated in experiment #10 pure SOA by homogeneous nucleation in the absence of seed aerosol (background particle concentration ~5 cm^{-3}). The reaction yielded a maximum of 1×10^5 cm^{-3} new particles (CNC count of particles with diameters $\geqslant 7$ nm) which decreased rapidly due to coagulation, while the count median diameter of the dominant mode shifted from 64 nm at $t = 0.03$ h to 150 nm at $t = 13.6$ h. Fig. 8 shows the extinction spectrum of the organic aerosol which was measured at $t = 1.33$ h. The extinction due to scattering in the near IR and visible range is weak owing to the small particle size. Above 350 nm

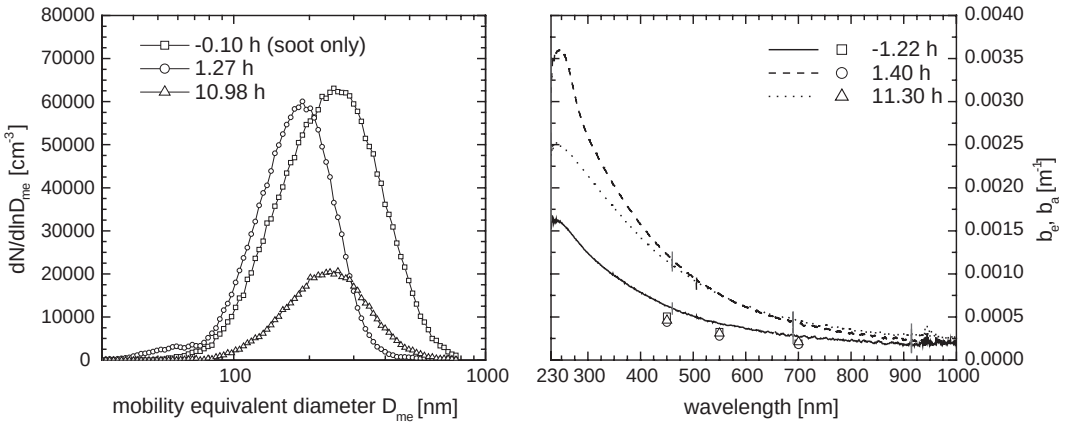

Fig. 9. Number size distribution of spark discharge soot before and after coating with SOA mass in experiment #9 (left). Note the *decrease* in particle size due to the collapse of the soot fractals. The corresponding extinction spectrum increases strongly due to the coating. By comparing the absorption coefficients (symbols) it is clear that this is mainly due to an enhanced scattering efficiency.

the spectrum agrees within the error limits with a Mie calculation based on the size distribution measured at $t = 1.23$ h and assuming spherical particles with $n = 1.44$. Below 300 nm extinction increases more strongly than predicted by Mie theory. The superimposed absorption, which was already observed before α-pinene is added, is due to the strong Hartley band of ozone with a maximum at 250 nm. The band cannot be completely eliminated by the reference-sample-reference cycling procedure, because ozone is partially destroyed on the particle filter.

The temporal evolution of the size distribution during experiment #9 (coating of spark generator soot) is displayed on the left panel of Fig. 9, while the second panel in Fig. 10 shows the evolution of the particle number density. The number density was 74500 cm^{-3} just before α-pinene was added at $t = -3$ min. As can be seen from Figs. 9 and 10, the aerosol number density was practically unaffected by the reaction, while both the size distribution and the extinction spectrum changed dramatically. Note that the size distribution of the coated aerosol (which shows that new particle formation was insignificant, consistent with the extreme weakness of the new particle mode below 100 nm) becomes more narrow and that the count median diameter *decreases* from 250 nm at $t = -0.1$ h to about 180 nm at $t = 1.3$ h after the reaction. The opposite behavior, namely an enhancement of the slow coagulation-induced growth rate due to coating, would have been expected for dense spherical seed particles, e.g. dry ammonium sulfate (Saathoff et al., 2003c). We conclude that the condensable ozonolysis products of α-pinene give rise to capillary forces in the small angle cavities of the agglomerates leading to more compact particles. This interpretation is supported by electron microscopy analysis of the soot agglomerates which clearly reveals the collapse and the formation of more compact particles due to the coating process (see Saathoff et al., 2003c). A similar decrease in the mobility equivalent diameter of Palas soot in the presence of water vapor has been observed by Weingartner, Burtscher, and Baltensperger (1997) over the whole range of relative humidities from less than 30 % to near 100 %.

The extinction spectrum of the spark generated soot aerosol increases strongly due to the coating with SOA mass (Fig. 9). Note that the additional enhancement of the extinction coefficient

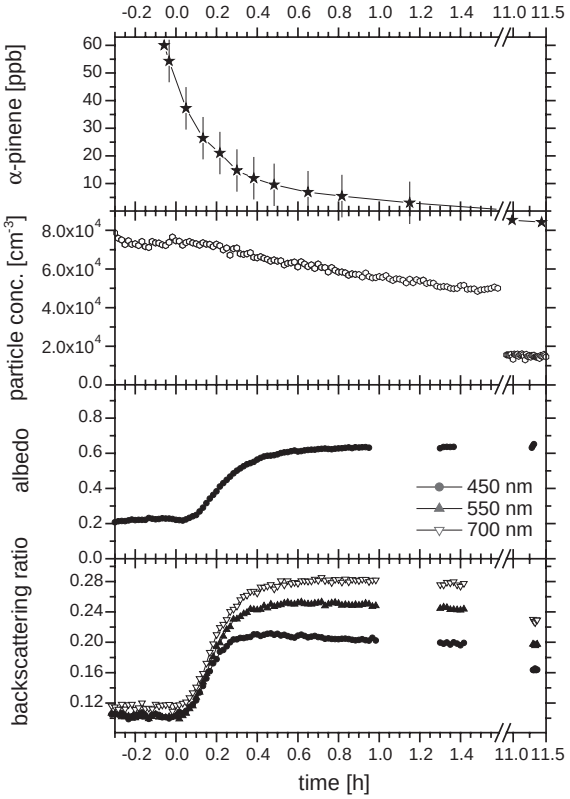

Fig. 10. Time evolution of the α-pinene concentration, the particle number density, the single scattering albedo at $\lambda = 450$ nm, and the backscattering ratio in experiment #9. Due to the large specific surface of the spark discharge soot new particle formation by homogeneous nucleation was not observed in this experiment. The dielectric coating leads to a strong increase of the scattering albedo. The increase of the backscattering ratio reflects the formation of more compact particles.

beyond 300 nm of the spectrum measured at 1.4 h is due to absorption by ozone as discussed above. Compared to the extinction spectrum the absorption coefficients of soot in the visible seem to be unaffected by the coating process, resulting in a strong increase of the single scattering albedo at 450 nm from 0.2 of the pure spark discharge soot to more than 0.6 after the coating (Fig. 10). Correlated with the scattering increase in Fig. 10, the backscattering ratio increases as well, reflecting the above transition from the fractal soot morphology to more compact, and thus smaller, particles. Since the SOA mass forms a permanent coating it is not yet possible to decide what fractions of the scattering and backscattering increase can be assigned to the particle restructuring and the dielectric coating.

At first glance the result of an unaffected absorption coefficient seems to be somewhat in contradiction to theoretical predictions of a strong absorption enhancement by encapsulating a soot core by a dielectric host as referred to in the introduction. Fig. 11 shows the temporal evolution of the absorption coefficient b_a during the coating process. We interpolated the nephelometer data to $\lambda = 473$ nm to evaluate b_a at this wavelength using the extinction cell data. Thus, b_a is actually not constant but

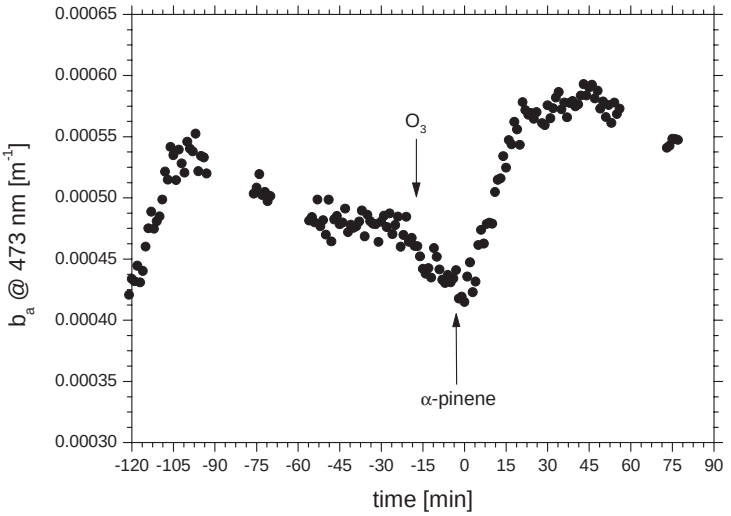

Fig. 11. Time dependence of the absorption coefficient of spark discharge soot during the coating with SOA mass in experiment #9. Plotted are the coefficients based on the extinction cell measurements at $\lambda = 473$ nm and the nephelometer measurements interpolated to this wavelength. After the end of soot admixing at $t = -105$ min the coefficient decreases due to mass losses. The time origin denotes the moment of α-pinene injection. The dielectric coating clearly enhances the absorption coefficient by roughly 35%. Note the slight but significant decrease of the absorption coefficient in the presence of ozone.

increases significantly during the coating process. On a time scale of 45 min which corresponds to roughly 90% breakdown of the α-pinene concentration, b_a increases from 4.3×10^{-4} to a value of 5.9×10^{-4} m^{-1}. Since the SOA coating has a dielectric optical behavior and assuming a negligible soot mass loss during that time this increase corresponds to an enhancement of the absorption cross section σ_a of about 35%. After the coating process the absorption coefficient starts to decrease which is certainly caused by the ongoing particle mass loss due to diffusion and sedimentation.

Saathoff et al. (2003c) estimated that the SOA coating of primaries is in the order of a few nanometers. The result of an absorption enhancement of a few ten percent due to this thin organic coating is in reasonable agreement with theoretical predictions by Fuller et al. (1999). They reported enhancement factors of more than two for coatings thicker than a few hundred nanometers. The optics of such thickly coated soot aerosol will be the focus of future investigations.

It is noteworthy that from Fig. 11 there is evidence for a slight decrease of b_a of spark discharge soot after admixing ozone to the chamber. This finding is well supported by the strong decrease of the photo emission signal of the particles measured simultaneously by a photoelectric aerosol sensor (Saathoff et al., 2003c). Since this signal is dominated by the composition of the soot surface, the result indicates that the oxidation of the soot surface by ozone may have a significant influence on the absorption cross section of atmospheric soot.

4.6. Comparison of the absorption coefficients with results obtained by the Integrating Plate Method (IPM)

The absorption coefficients measured offline by the IPM are compared in Fig. 12 with the respective coefficients measured by the difference method (DM). Since the time span between the IPM filter

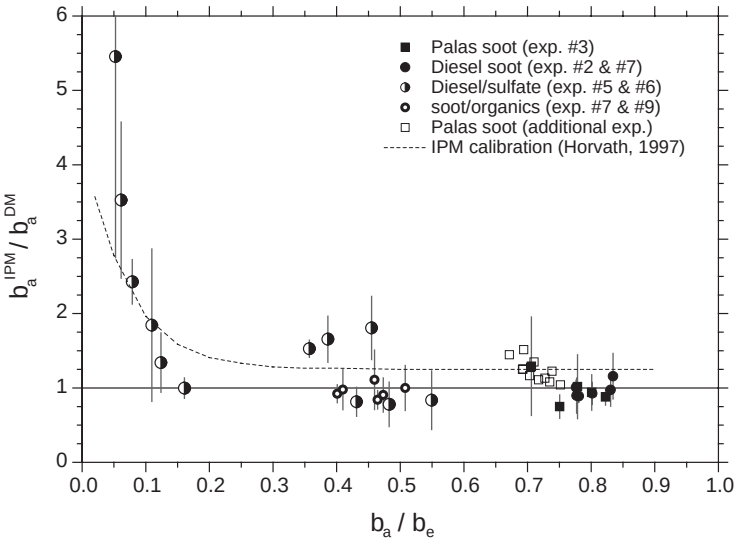

Fig. 12. Comparison of the absorption coefficients determined by the integrating plate method (IPM) and by the difference method (DM) as function of the absorption-to-extinction ratio b_a/b_e. The dashed line summaries the result of a laboratory study performed by Horvath (1997) for different internal and external mixtures of carbon aerosol with a non-absorbing aerosol (sugar).

sampling and the DM measurement was not in all cases short enough to avoid mass loss errors, only coefficients measured within a reasonable time span are compared in Fig. 12. Furthermore, the data are compared as measured, without any corrections. As found by Horvath (1997) the absorption coefficient determined by the IPM depends on the absorption-to-extinction ratio b_a/b_e of the aerosol especially for small values of this ratio. This is due to the increased path length within the deposited aerosol layer induced by multiple scattering. For the pure soot filter samples the two independent methods yield absorption coefficients which agree quite well.

The large fraction of sulfate aerosol in experiment #6 leads to a strong increase of the path length within the deposited aerosol layer and thus to an overestimation of the absorption coefficient by IPM up to a factor of 5.5. For those small b_a/b_e ratios the accuracy of the DM decreases drastically reflected by the large error bars in Fig. 12. In experiment #5 the masses of Diesel soot and ammonium sulfate aerosol were approximately equal resulting in intermediate b_a/b_e values. The initial IPM absorption coefficient overestimates the "true" value by roughly 50% whereas an underestimation of $\sim$20% is deduced at the end of the experiment. Interestingly the same trend is found for the two IPM measurements of experiment #6 (Fig. 12). The IPM analysis of the two soot coating experiments yields absorption coefficients which agree quite well with the respective values deduced by the DM.

The IPM has been designed for atmospheric measurements where absorption-to-extinction ratios between 0.07 and 0.3 (single scattering albedo between 0.7 and 0.93) are frequent. In this range the calibration by Horvath (1997) reflects the experimental data quite well. However, the data base is surely too narrow to draw more substantial conclusions about the quality of the IPM calibration.

5. Conclusions

The visible mass specific extinction (absorption) cross section of Diesel soot is by a factor of two higher than that of spark discharge soot. In conjunction with the different positions of the π-electronic band maxima in the mid-UV and results by HRTEM analysis this difference can be attributed to distinct solid state structures of the two soot materials. This is also reflected by the different refractive indices deduced from the measurements by applying the simple RDG approximation for the optics of the fractal soot aggregates. Interestingly, at $\lambda = 550$ nm these indices mark the upper and lower limits of the range of soot refractive indices found in the literature, as compiled by Fuller et al. (1999). Thus, concerning the optical properties, spark discharge soot is not a good proxy for atmospheric soot. This should be taken into account when calibrating soot sensors based on the extinction or absorption cross sections of soot. Furthermore, the optical cross sections of soot exhibit a rather strong wavelength dependence which is partly due to the wavelength dependence of the refractive index, and which is sometimes neglected in inter-comparisons of measurements gathered by different optical methods. Since the extinction cross section of soot is not affected significantly by self-coagulation, at least for larger aggregates, the extinction coefficient is a good measure for the soot mass concentration in pure soot aerosol.

The coagulation dynamics of soot can be modeled quite well by the coagulation code COSIMA. An optics module based on the RDG approximation was implemented in the COSIMA code allowing the modeling of the temporal evolution of the absorption and scattering coefficients. Good agreement between the measured and modeled single scattering albedos was found for both soot types on a time scale of two days.

Internal mixing of Diesel soot and dry $(NH_4)_2SO_4$ aerosol was partially achieved by a two-day coagulation experiment in the AIDA chamber. An upper limit of a few ten percent for the number fraction of internally mixed particles was estimated by single particle mass spectroscopy (Kirchner et al., 2003) and HRTEM (Wentzel et al., 2003). Such mixing conditions cause no measurable enhancement in the absorption cross section of the ensemble in good agreement with theoretical considerations which predict an absorption enhancement factor of only 1.04 for a totally internal mixture. Thus, for internal mixing by coagulation with dry sulfate aerosol the absorption coefficient is still a good measure for the soot mass concentration.

The oxidation of α-pinene by an excess of ozone leads to low volatile secondary organic compounds which nucleate heterogeneously in the presence of spark discharge soot to form a dielectric coating. A SOA/soot mass ratio around 0.6 was achieved in the experiment. Due to the large specific surface area of spark generated soot homogeneous nucleation of the oxidation products was not observed in the presence of soot aerosol. The coating process causes a collapse of the soot aggregates which was proved by the decrease of the mobility equivalent diameter of the coated aggregates. As a result of the change in effective size the hemispheric backscattering ratio increases by a factor of 2.5 from 0.10 to 0.25 at $\lambda = 550$ nm. Furthermore, the thin dielectric coating of a few nanometers causes a strong increase of the single scattering albedo from 0.2 to 0.6 at $\lambda = 450$ nm. Thus, the visible backscattering albedo of soot strongly increases by a factor as high as 7.5 due to the organic coating.

The specific absorption cross section of spark generated soot is also enhanced by the thin organic coating. A significant increase of the absorption coefficient of roughly 35% was observed during the coating process. This supports the theoretical prediction that the most recent assessment of the

positive global forcing by black carbon aerosols (IPPC, 2001) should be revised to include the absorption enhancement effect (Jacobson, 2001). Further experimental investigations with coatings of different thickness and coating materials (e.g. H_2SO_4) are necessary to assess these effects.

Acknowledgements

This work was conducted with financial support by BMBF under grant (AFS 07AF209). The authors thank E. Kranz for performing the aerosol mass analysis by CO_2 coloumetry and ion chromatography. R. Buschbacher and G. Scheurig are thanked for their support during the experiments and the subsequent data analysis. We appreciate that D. Mackowski, K. Fuller, and M. Mishchenko have been making their multiple sphere scattering code available to the public.

References

Ballach, J., Hitzenberger, R., Schultz, E., & Jaeschke, W. (2001). Development of an improved optical transmission technique for black carbon (BC) analysis. *Atmospheric Environment*, *35*, 2089–2100.

Bohren, C. F., & Huffman, D. R. (1983). *Absorption and scattering of light by small particles*. New York: Wiley.

Charlson, R. J., Schwartz, S. E., Hales, J. M., Cess, R. D., Coakley, J. A., Hansen, J. E., & Hofmann, D. J. (1992). Climate forcing by anthropogenic aerosols. *Science*, *255*, 423–430.

Colbeck, I., Atkinson, B., & Johar, Y. (1997). The morphology and optical properties of soot produced by different fuels. *Journal of Aerosol Science*, *28*, 715–723.

Dobbins, R. A., & Megaridis, M. (1991). Absorption and scattering of light by polydisperse aggregates. *Applied Optics*, *30*, 4747–4754.

Dobbins, R. A., Mulholland, G. W., & Bryner, N. P. (1994). Comparison of a fractal smoke optics model with light extinction measurements. *Atmospheric Environment*, *28*, 889–897.

Farias, T. L., Köylü, Ü. O., & Carvalho, M. G. (1996). Range of validity of the Rayleigh–Debye–Gans theory for optics of fractal aggregates. *Applied Optics*, *35*, 6560–6567.

Fuller, K. A., Malm, W. C., & Kreidenweis, S. M. (1999). Effects of mixing on extinction by carbonaceous particles. *Journal of Geophysical Research*, *104*, 15,941–15,954.

Hansen, J., Sato, M., Ruedy, R., Lacis, A., & Oinas, V. (2000). Global warming in the twenty-first century: An alternative scenario. *Proceedings of the National Academy of Sciences of the United States of America*, *97*, 9875–9880.

Henning, Th., & Schnaiter, M. (1998). Carbon—from space to laboratory. *Earth, Moon and Planets*, *80*, 179–207.

Horvath, H. (1995). Size segregated light absorption coefficient of the atmospheric aerosol. *Atmospheric Environment*, *29*, 875–883.

Horvath, H. (1997). Experimental calibration for aerosol light absorption measurements using the integrating plate method-summary of the data. *Journal of Aerosol Science*, *28*, 1149–1161.

Intergovernmental Panel on Climate Change, (IPCC). (2001). *Climate change 2001*. In J. T. Houghton, Y. Ding, D. J. Griggs, M. Noguer, P. J. van der Linden, & D. Xiaosu (Eds.), *The scientific basis*. Cambridge, UK: Cambridge University Press.

Jacobson, M. Z. (2001). Strong radiative heating due to the mixing state of black carbon in atmospheric aerosols. *Nature*, *409*, 695–697.

Jäger, C., Henning, Th., Schlögl, R., & Spillecke, O. (1999). Spectral properties of carbon black. *Journal of Non-Crystalline Solids*, *258*, 161–179.

Krämer, L., Bozoki, Z., & Niessner, R. (2001). Characterisation of a mobile photoacoustic sensor for atmospheric black carbon monitoring. *Annals of Science*, *17*, s563–s566.

Kirchner, U., Vogt, R., Natzeck, C., & Goschnik, J. (2003). Single particle MS, SNMS, SIMS, XPS, and FTIR spectroscopic analysis of soot particles during the AIDA campaign. *Journal of Aerosol Science*, *34*, 1323–1346.

Klein, K. F., Schließmann, P., Smolka, E., Hillrichs, G., Belz, M., Boyle, W. J. O., & Grattan, K. T. V. (1997). UV-stabilized silica-based fibre for applications around 200 nm wavelength. *Sensors and Actuators B*, *38–39*, 305–309.

Lide, D. R. (Ed.) (1999). *CRC handbook of chemistry and physics*. Cleveland, OH: Chemical Rubber Company (CRC) Press.

Liousse, C., Cachier, H., & Jennings, S. G. (1993). Optical and thermal measurements of black carbon aerosol content in different environments: Variation of the specific attenuation cross section, sigma (σ). *Atmospheric Environment A*, *27*, 1203–1211.

Mackowski, D. W. (1994). Calculation of total cross sections of multiple sphere clusters. *Journal of the Optical Society of America A*, *11*, 2851–2861.

Mennella, V., Colangeli, L., Bussoletti, E., Monaco, G., Palumbo, P., & Rotundi, A. (1995). On the electronic structure of small carbon grains of astrophysical interest. *Astrophysical Journal, Supplement Series*, *100*, 149–157.

Michel, B., Henning, Th., Jäger, C., & Kreibig, U. (1999). Optical extinction by spherical carbonaceous particles. *Carbon*, *37*, 391–400.

Moosmüller, H., Arnott, W. P., Rogers, C. F., Chow, J. C., & Frazier, C. A. (1998). Photoacoustic and filter measurements related to aerosol light absorption during the Northern Front Range Air Quality Study (Colorado 1996/1997). *Journal of Geophysical Research*, *103*, 28149–28157.

Mulholland, G. W., & Mountain, R. D. (1999). Coupled dipole calculation of extinction coefficient and polarization ratio for smoke agglomerates. *Combustion and Flame*, *119*, 56–68.

Naumann, K.-H. (2003). COSIMA—a computer program simulating the dynamics of fractal aerosols. *Journal of Aerosol Science*, *34*, 1371–1397.

Papoular, R., Conrad, J., Guillois, O., Nenner, I., Reynaud, C., & Rouzaud, J.-N. (1996). A comparison of solid-state carbonaceous models of cosmic dust. *Astronomy & Astrophysics*, *315*, 222–236.

Petzold, A., Kopp, C., & Niessner, R. (1997). The dependence of the specific attenuation cross-section on black carbon mass fraction and particle size. *Atmospheric Environment*, *31*, 661–672.

Raes, F., van Dingenen, R., Vignati, E., Wilson, J., Putaud, J.-P., Seinfeld, J. H., & Adams, P. (2000). Formation and cycling of aerosols in the global troposphere. *Atmospheric Environment*, *34*, 4215–4240.

Robertson, J., & O'Reilly, E. P. (1987). Electronic structure of amorphous carbon. *Physics Review B*, *35*, 2946–2957.

Saathoff, H., Möhler, O., Schurath, U., Kamm, S., Dippel, B., & Mihelcic, D. (2003a). The AIDA Soot Characterisation Campaign 1999. *Journal of Aerosol Science*, *34*, 1277–1296.

Saathoff, H., Naumann, K.-H., Schnaiter, M., Schöck, W., Weingartner, E., Baltensperger, U., Krämer, L., Bozoki, Z., Pöschel, U., Niessner, R., & Schurath, U. (2003b). Carbon mass determinations during the AIDA Soot Aerosol Campaign 1999. *Journal of Aerosol Science*, *34*, 1399–1420.

Saathoff, H., Naumann, K.-H., Schnaiter, M., Schöck, W., Möhler, O., Schurath, U., Weingartner, E., Gysel, M., & Baltensperger, U. (2003c). Coating of soot and $(NH_4)_2SO_4$ particles by ozonolysis products of α-pinene. *Journal of Aerosol Science*, *34*, 1297–1321.

Schnaiter, M., Mutschke, H., Dorschner, J., Henning, Th., & Salama, F. (1998). Matrix-isolated nano-sized carbon grains as an analog for the 217.5 nanometer feature carrier. *Astrophysical Journal*, *498*, 486–496.

Sorensen, C. M., Cai, J., & Lu, N. (1992). Light-scattering measurements of monomer size, monomers per aggregate, and fractal dimension for soot aggregates in flames. *Applied Optics*, *31*, 6547–6557.

Toon, O. B., Pollack, J. B., & Khare, B. N. (1976). The optical constants of several atmospheric aerosol species: Ammonium sulfate, aluminum oxide, and sodium chloride. *Journal of Geophysical Research*, *81*, 5733–5748.

Weingartner, E., Burtscher, H., & Baltensperger, U. (1997). *Atmospheric Environment*, *31*, 2311–2327.

Weingartner, E., Saathoff, H., Schnaiter, M., Streit, N., Bitnar, B., & Baltensperger, U. (2003). Absorption of light by soot particles: Determination of the absorption coefficient by means aethalometers. *Journal of Aerosol Science*, *34*, 1445–1463.

Wentzel, M., Gorzawski, H., Naumann, K.-H., Saathoff, H., & Weinbruch, S. (2003). Transmission electron miscroscopical and aerosol dynamical characterisation of soot aerosols. *Journal of Aerosol Science*, *34*, 1347–1370.